ORNL/SPR-2021/2100

HFIR SiC-SiC Composite Clad Tube Bowing Test: Pre-Irradiation Characterization

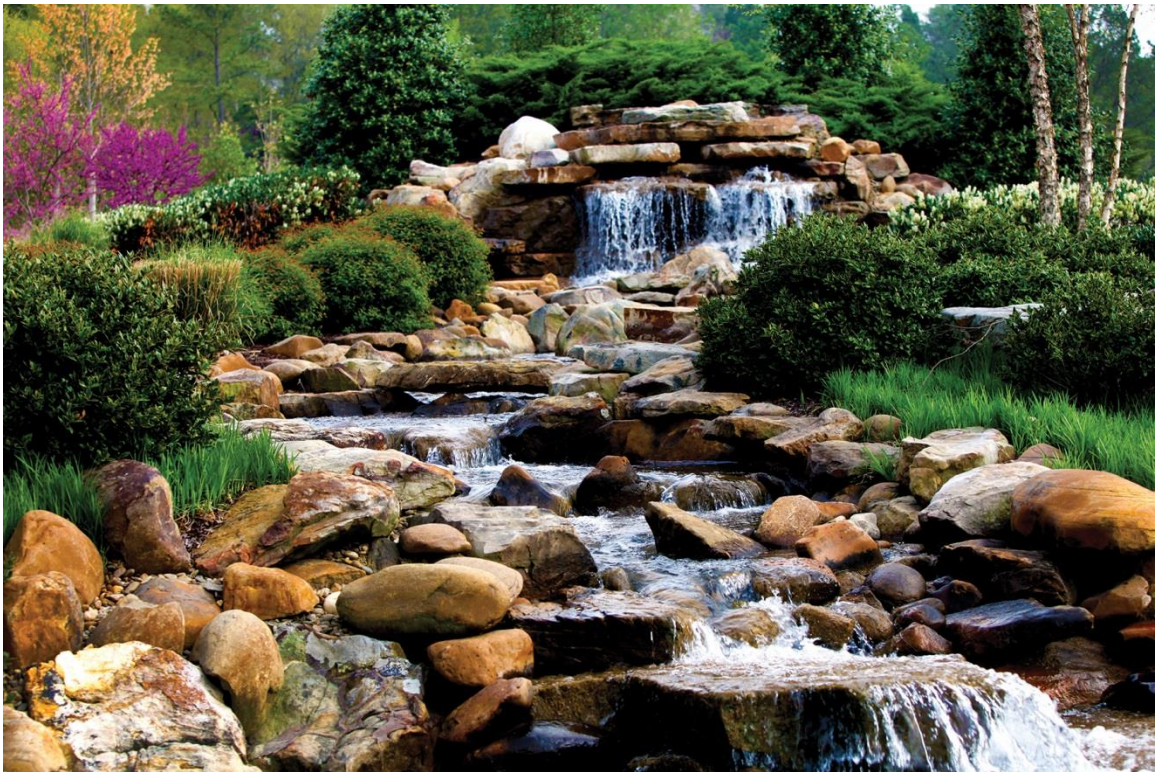

Josina W. Geringer
Chris Petrie
Adam James
Takaaki Koyanagi
Christian Deck
Yutai Katoh

August 2021

OAK RIDGE National Laboratory

ORNL IS MANAGED BY UT-BATTELLE LLC FOR THE US DEPARTMENT OF ENERGY

ORNL/TM-2021/2100

Material Science and Technology Division

HFIR SIC-SIC COMPOSITE CLAD TUBE BOWING TEST: PRE-IRRADIATION CHARACTERIZATION

Josina W. Geringer
Chris Petrie
Adam James
Takaaki Koyanagi
Christian Deck
Yutai Katoh

August 2021

Prepared by
OAK RIDGE NATIONAL LABORATORY
Oak Ridge, TN 37831-6283
managed by
UT-BATTELLE, LLC
for the
US DEPARTMENT OF ENERGY
under contract DE-AC05-00OR22725

CONTENTS

LIST OF FIGURES

LIST OF TABLES

ABBREVIATIONS

Al	Aluminum
DOE	U.S. Department of Energy
EOC	end of cycle
HFIR	High Flux Isotope Reactor
HNLS	Hi-Nicalon Type-S
ORNL	Oak Ridge National Laboratory
SiC-SiC	silicon carbide – silicon carbide
VXF	Vertical Experiment Facility
Zr	zirconium

ACKNOWLEDGEMENTS

This study was supported by the US Department Energy's (DOE's) Office of Nuclear Energy for the Advanced Fuels Campaign of the Nuclear Technology R&D program and the Westinghouse Electric Corporation/General Atomics Funding Opportunity Announcement program under contact DE-AC05-00OR22725 with Oak Ridge National Laboratory (ORNL) managed by UT Battelle LLC. A portion of this research used resources at the High Flux Isotope Reactor, a DOE Office of Science User Facility operated by ORNL. Annabelle Le Coq assisted with specimen preparation, and David Bryant (ORNL) performed the specimen engraving and experiment assembly. T. M. (Tom) Rosseel and Lauren Garrison (ORNL) performed technical reviews of the report and provided helpful comments.

SUMMARY

This report describes the pre-irradiation characterization of the SiC-SiC composite clad tube bowing experiment that will be irradiated in the High Flux Isotope Reactor (HFIR). There are concerns that SiC-SiC fuel cladding in light water reactors could undergo bowing because of the non-uniform fast neutron flux profiles. This experiment is combined with the SiC-SiC channel box experiment, which has similar concerns regarding control blade movements in boiling water reactors. The HFIR experiment aims to validate the predicted deformation and stresses in the composite clad specimen after the exposure of fast neutron flux gradients. Significant radial fast neutron flux gradients that exist in the permanent reflector of HFIR were thoroughly characterized by using detailed 3D neutronic calculations. The 3D displacement damage dose rate profile and the resulting volumetric swelling in SiC were used as inputs to structural analyses to determine the predicted deformation that will affect the specimens.

The tube specimens were characterized by using traditional dimensional inspection and surface profilometry to provide detailed information regarding the pre-irradiation condition as the first step to evaluate the radiation-induced deformation. Furthermore, fine engraving markers were inscribed along all outer surfaces of the specimen and mapped by using a digital microscope and a multidimensional stage. This allows marker spacings to be accurately measured and compared with similar measurements that will be made post-irradiation to provide local radiation-induced strain mapping. The experiment successfully completed two HFIR cycle irradiations, cycles 492 and 493, which finished on July 25, 2021.

1. INTRODUCTION

This report summarizes the results of the pre-irradiation characterization of the SiC-SiC composite clad tube specimens from the joint research venture between Westinghouse-General Atomics and the Advanced Fuels Campaign Program. This report studied the effect of bowing due to the exposure of fast neutron flux gradient along the height of the reactor. The irradiation was performed in the flux trap of the Oak Ridge National Laboratory High Flux Isotope Reactor (HFIR). This report includes the basics of the program (i.e., material, properties, and irradiation) and the results of the predicted property changes due to different irradiation conditions (i.e., temperature and total fluence).

SiC-SiC composites undergo temperature-dependent swelling under fast neutron irradiation (E > 0.1 MeV) [1]. Under flux gradients or non-isothermal irradiation, nonuniform swelling in SiC-SiC fuel cladding is expected to lead to lateral bowing or distortion, as previously shown [2]. An experiment was designed in HFIR to separate the temperature-dose-dependent effects that target a steady coolant temperature to validate the modeled lateral bowing as a result of the fast neutron exposure over the height (i.e., axial profile) of the reactor core.

The work presented herein primarily focuses on the anticipated distortion of a SiC-SiC composite tube for light water reactor fuel cladding applications. The evaluation is based on the composite behavior that surrounds the UO_2 fuel element. A typical fuel clad component is ~10 mm in diameter and ~4 m long. Because of temperature-dependent swelling and fast neutron flux gradients, bowing of the cladding components can obstruct control rod insertion or block coolant channels.

This report is a partial reporting of the combined channel box irradiation experiment, which investigated the lateral bowing of the miniature channel box used in boiling water reactors, as well as cladding tubes used in light water reactors due to differential swelling. The stress analysis and flux calculations were reported elsewhere [2, 3].

Promising material properties—such as low neutron absorption, excellent high-temperature strength, maintained mechanical properties, and chemical inertness—and exceptional resistance to steam oxidation at high temperatures makes SiC-SiC an ideal candidate material to replace current Zr-alloy materials. However, SiC swelling and thermal conductivity are critical parameters for the feasibility of the application as determined by Lee [4] after modeling a multilayered SiC clad. In another study, Singh investigated the thermal-mechanical behavior of SiC-SiC and the combined interaction of the fuel rod [2]. Lee also concluded that irradiation-induced swelling in the SiC-SiC clad contributes significantly to the stress development model. The strain associated with the differential swelling as a result of differential flux and temperature profile dominate the stress profile in the cladding.

The dose-dependent swelling effects is well known and well documented [5–10]. Using the swelling rate model [9], Katoh [10] separated the swelling effects as a function of dose and temperature.

Separating the induced temperature-dose effects—even with rudimentary methods—allows for independent property characterization that can be validated through experimentation. It also provides a baseline to model the lateral bowing due to the fast flux gradient.

The purpose of this experiment is to examine the lateral bowing behavior of the composite clad tube caused by the differential swelling under fast neutron irradiation at a 50–60°C coolant temperature. This report discusses the pre-irradiation work performed to characterize the SiC-SiC composite tube specimens.

2. EXPERIMENT DESIGN

The irradiation experiment was designed for HFIR's large Vertical Experiment Facility (VXF) in the HFIR reflector, as shown in Figure 1 [11]. The experiment design allows the specimens to be directly cooled by the reactor coolant, which flows through the experiment from top to bottom. The coolant temperature range is between 50 to 60°C.

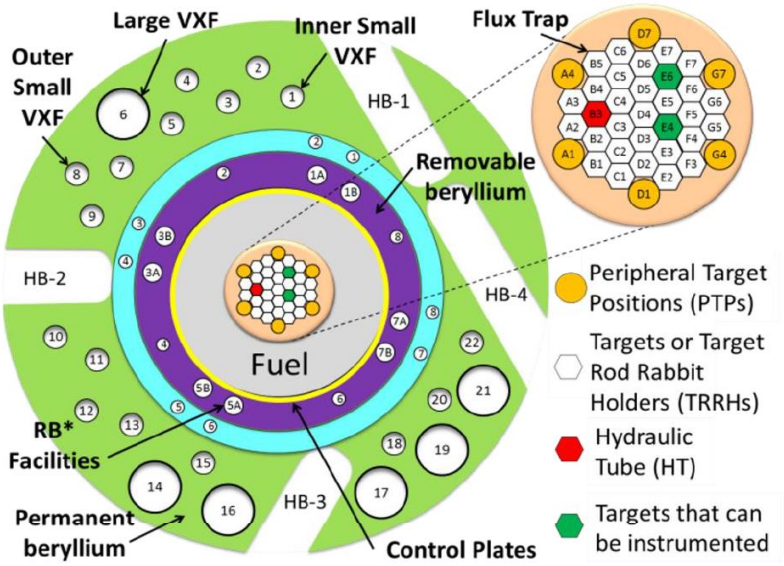

Figure 1. Experiment positions in HFIR.

Figure 2 shows the irradiation experiment design and assembly. The irradiation vehicle is a two-piece Al holder that results in a cylindrical assembly with internal cutouts for the specimens when welded together. The orifice at the bottom of the holder controls the coolant flow rate that enters from the top of the experiment. The miniature channel box and tube specimens are assembled inside the holder cutout. The nominal dimensions of the miniature channel box are 30 mm × 30 mm × 380 mm with a 1.25 mm thick wall. As previously mentioned, this irradiation is a shared programmatic activity, and the pre-irradiation characterization of the channel box specimen is reported elsewhere [12].

The tube specimens have a prototypic pressurized water reactor cladding diameter of 9.5 mm, a wall thickness of 1 mm, and a length of 380 mm. Two Al internal supports, lower and upper, are stacked together on either end of the channel box and secured by using a tie rod. The large features at the top and bottom of the support pieces ensure that the channel box remains centered inside the Al holder. Wave springs are placed between the channel box specimen and the supports to keep the channel box centered around the support pieces. The wave springs have minimal stiffness to allow the channel box to bow without applying any significant load or stress on the channel box. Radial holes at the top and bottom of the tube specimens allow them to be secured to the internal supports by using fasteners. The fasteners pass through the tube specimens and slots in the slotted pins, which are welded to the internal supports. This allows the tube specimens to bend and translate axially while maintaining their orientation inside the experiment. The specimens were assembled with their engraved IDs ("01" and "22") pointing toward the bottom of the experiment. Specimen 01 is in the position closer to the core, while tube specimen 22 is positioned further from the core.

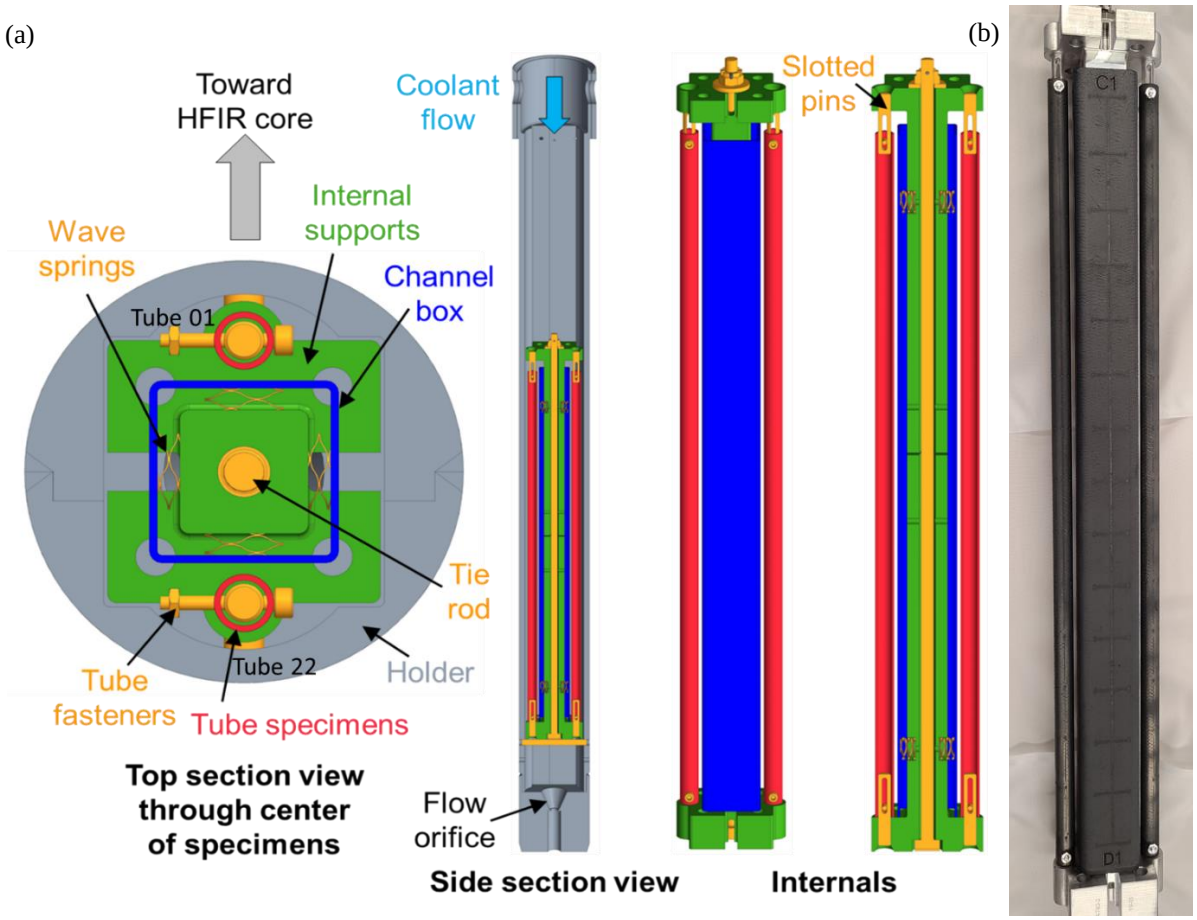

Figure 2. The (a) design and (b) assembly of the 380 mm long tube specimens in the channel box experiment.

Figure 3 shows the expected dose at the end of cycle (EOC) for various radial distances (*Y*), assuming the midplane ($Y = 0$) to be the center of the large VXF location. The dose reduces significantly when moving away from the core (decreasing *Y*). Beginning-of-cycle and EOC comparisons showed that there were no significant dose differences. The calculated dose is derived from the fast neutron fluence with a relationship where 1 dpa equals 1×10^{25} n/m^2, and $E > 0.1$ MeV.

As reported elsewhere [12], the dose was converted to volumetric swelling by using literature data from previous HFIR irradiation experiments performed at the same coolant temperatures. Figure 4 [13] demonstrates the anticipated swelling gradients across the channel box experiment and partially shows the gradient across the tube specimens. The red and blue lines indicate the tube specimen positions relative to the radial midplane ($Y = 0$) in the experiment assembly. The profile shows the midplane position of the core (where $Z = 0$) after one cycle.

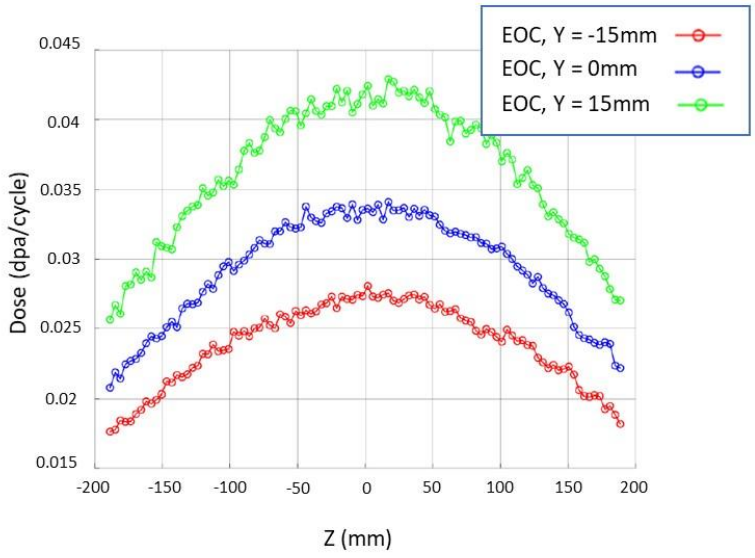

Figure 3. Dose per cycle (EOC) as a function of axial position *X* with radial position *Y* as a parameter.

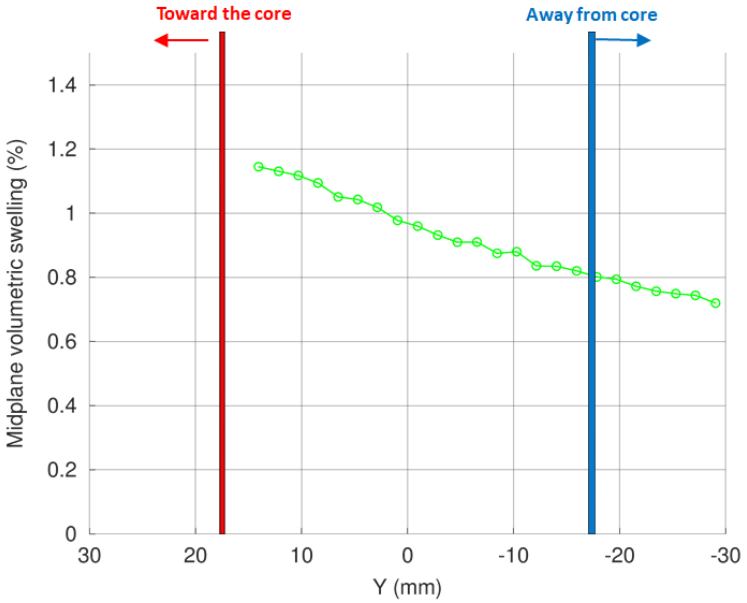

Figure 4. Spatial swelling gradients over the experiment at core midplane after one irradiation cycle. The vertical lines indicate the positions of the tube specimens in the experiment position.

The displacement analysis of the SiC-SiC tube specimens was performed by using the commercial Ansys software. The displacement analysis is based on the calculated temperature and flux boundary conditions mentioned previously. The variation in the volumetric swelling between the front and back of the specimens (when facing the core) creates lateral strain along the length of the specimens. The simulated displacement, U_Y, (in meters), as illustrated in Figure 5, shows the combined result of the of lateral swelling and bowing effects. The visual illustration is artificially magnified by a factor 10 but the reported scales are the true calculated displacement values. The lateral bow is defined as the maximum lateral displacement for all nodes at a given Z position relative to the maximum lateral displacement at $Z = 0$ mm and compensates for swelling so that the lateral displacement will be slightly larger than the anticipated lateral bowing.

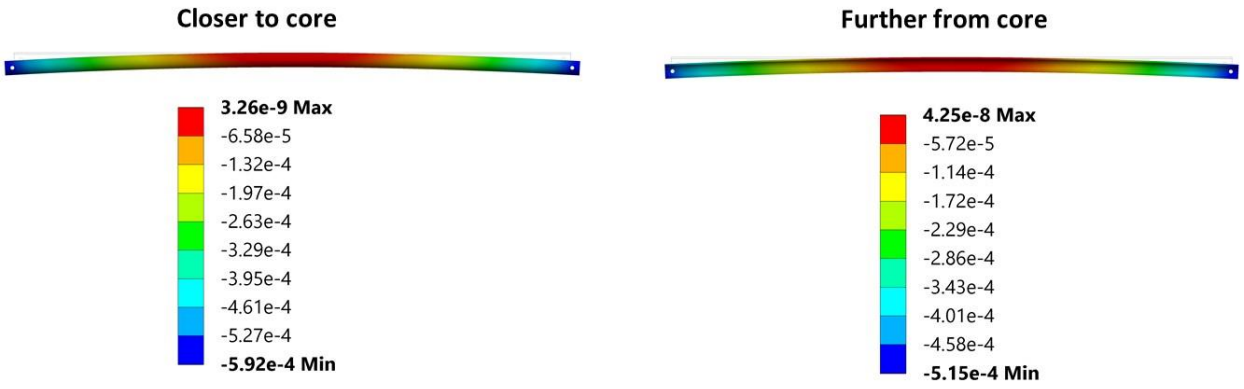

Figure 5. Simulated displacement (in meters) after one HFIR cycle. The visual deformation of the structures are artificially magnified by a factor 10.

From earlier experiments, the volumetric swelling was determined to range from 0.7 to 1.15% after one HFIR cycle with dose values ranging from 0.02 to 0.04 dpa at coolant temperature. This corresponds to linear strains ranging from 0.23 to 0.38%. After a second HFIR cycle, the volumetric swelling ranges from 1.15 to 1.9% with dose values ranging from 0.04 to 0.08 dpa at coolant temperature. Figure 6 shows the expected maximum trend of the tube specimen displacement for the radial direction (*Y*) and the expected bowing to occur after each HFIR cycle.

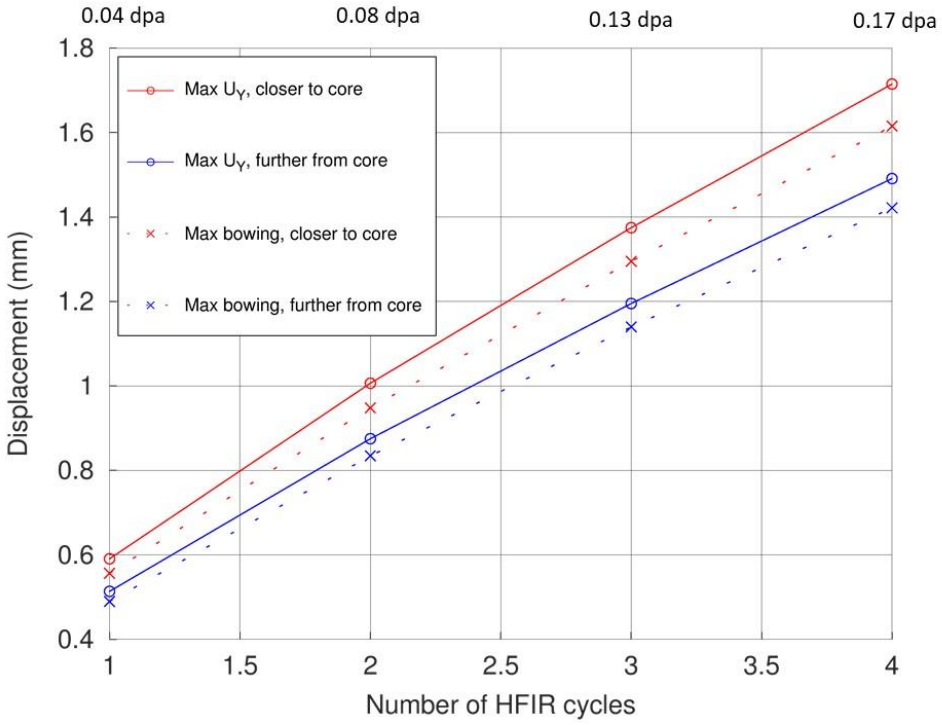

Figure 6. Simulated maximum tube specimen displacement in the *Y* direction (U_Y) and bowing vs. number of HFIR cycles.

3. SPECIMEN PREPARATION

3.1 SPECIMEN FABRICATION

The two SiC-SiC tube specimens with engraved IDs of 01 and 22 were fabricated by General Atomics and are hereafter designated as *T01* and *T22*, respectively. The specimens were fabricated with similar composition and processing. The fabrication used a Hi-Nicalon Type-S (HNLS) SiC fibers with a 150 nm thick pyrolytic C interphase surrounded by a SiC matrix formed by chemical vapor infiltration and a thin outer layer formed by using chemical vapor deposition. The two specimens have the same braided fiber architecture (Figure 7) with a ±50° braiding angle. The nominal fiber volume fraction was 30–40%. Figure 8 shows the two specimens. Two radial pin holes were machined at the ends of each specimen.

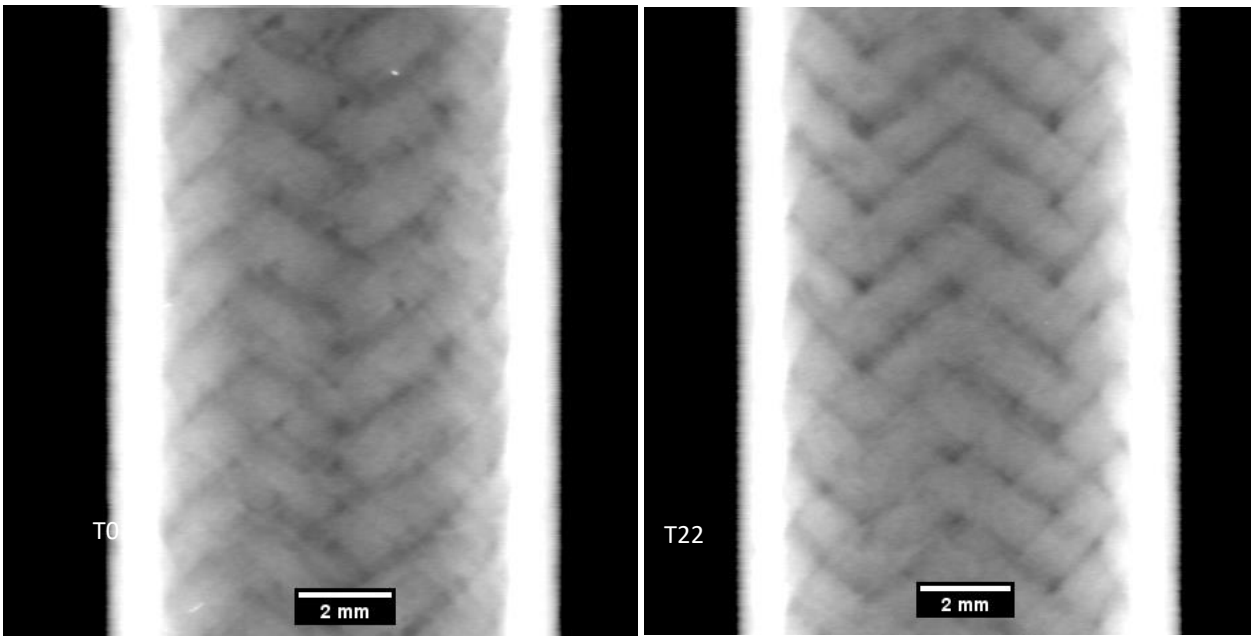

Figure 7. A 2D radiograph taken from T01 and T22 showing the fiber architecture pattern.

Figure 8. The two 380 mm HNLS SiC-SiC specimens.

3.2 SPECIMEN ENGRAVING

Each specimen was clearly marked to retain orientation and to duplicate setup for measurements before and after irradiation. Each specimen was engraved with eight dashed lines every 45° along the length of the specimen. Fine fiducial "x" markings separated by ~25 mm, were made in circled locations between the dashed lines, including at the start and end, along the length of each dashed line. The specimens were inscribed with an ID on one end, and a series of numbers 1–8, were engraved around the circumference to identify the individual dashed lines on the other end. This is also referred to as the perimeter number, P_x,

used in the remainder of the report. The line width of the fiducial markings was ~30µm. The center of each line must be located before and after irradiation to accurately determine displacements. Figure 9 shows the engraved schematic as described, and Figure 10 shows an example of specimen T01 with the 0° position (P_1, dashed line 1).

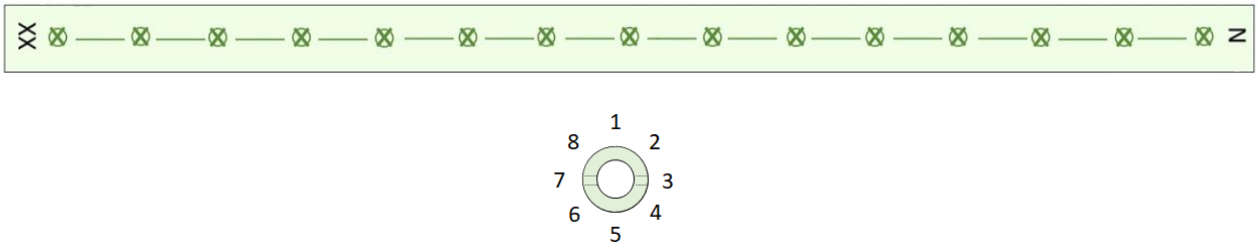

Figure 9. Engraving schematic.

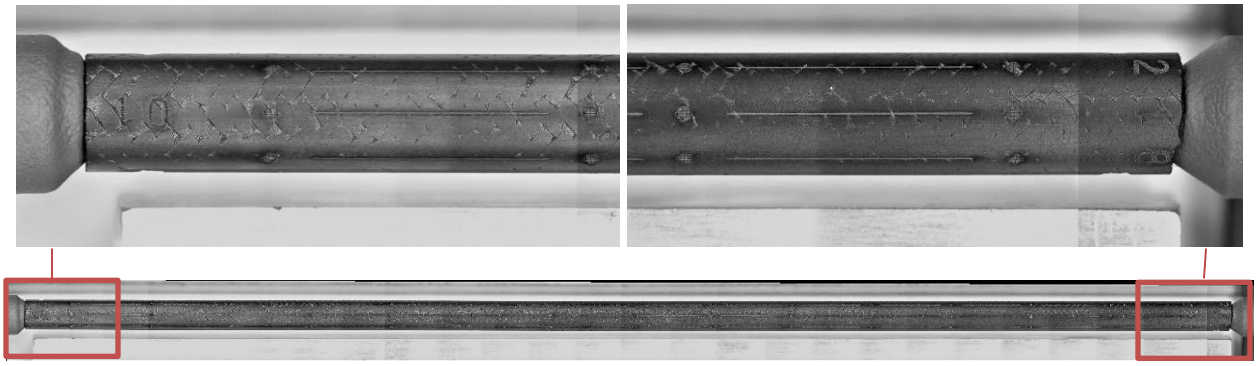

Figure 10. Example of the engraved specimen T01 (bottom) showing the enlarged section of the engraved ID 01 (top left) with fiducial marks, as well as the dashed lines and associated perimeter number (top right).

4. CHARACTERIZATION METHODS

4.1 SPECIMEN INSPECTION

The specimens were inspected for mass, dimensions, and straightness. The mass was taken by using a Mettler AE 240 S/N X207039, and the dimensions were measured by using Trimos Height Gage S/N 0081889 for length, Outside Micrometer S/N M212643 for diameter, and a Poly Micrometer S/N M212649 for thickness. The straightness was measured with a Mitutoyo Indicator S/N M212552.

The eight length measurements every 45° were taken along each identified perimeter location, as shown in Figure 11(a). Four diameter measurements, as shown in Figure 11(b), were taken at five positions along the length: the first at the top (ID or D1 location), the last at the bottom (perimeter number or D5 location), and three measures in between, as shown in Figure 11(c). Eight thickness measurements were taken at both the top and bottom of each marked perimeter line. The straightness was measured by rotating the specimens and obtaining the deviation from the set reference point. The reference, P_1-3, was set by placing the indicator in the center of the tube touching the engraved line "1." The tube ends were held in a stable position as the tubes were rotated.

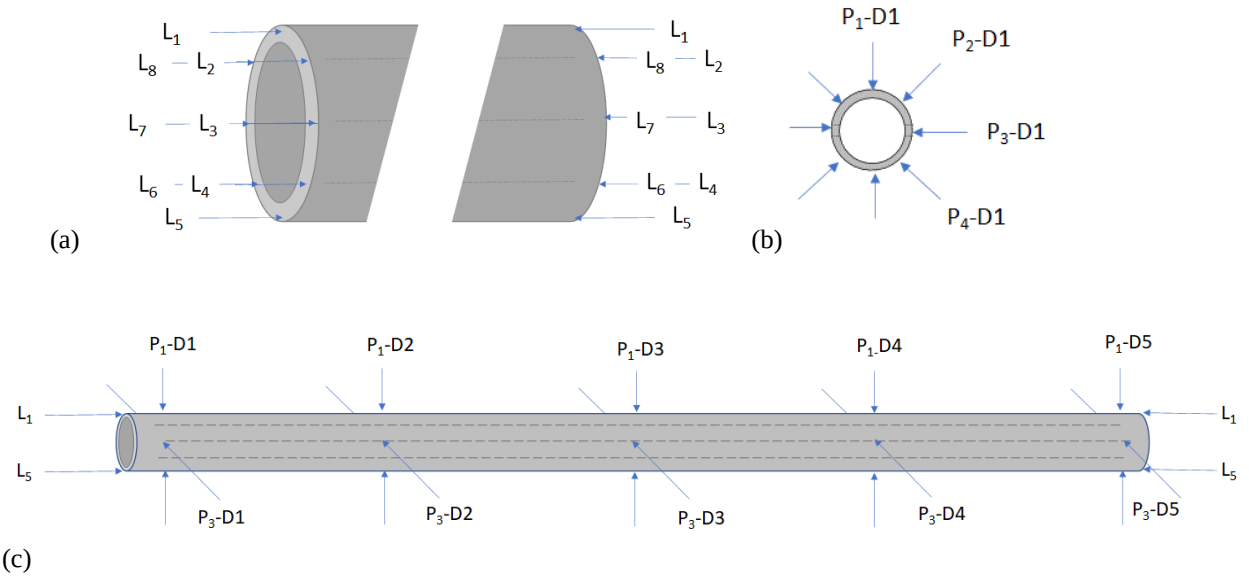

Figure 11. (a) Dimensional inspection labeling points for length measurements, (b) diameter measurements around the perimeter, and (c) diameter measurements over the span of the length.

4.2 TRANSLATIONAL STAGE SYSTEM

A custom 3D, four-directional, remote-controlled translational stage system was assembled to photograph, profile, and strain map the specimens. The system was assembled by using a combination of Thorlabs and Zaber equipment, and the setup is shown in Figure 12.

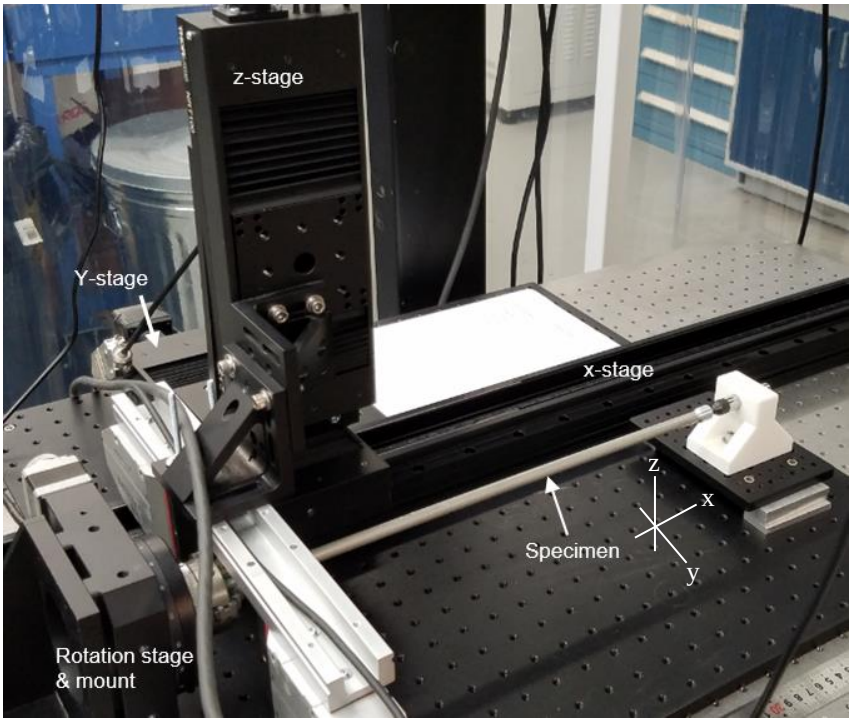

Figure 12. Custom translational stage system setup.

The Thorlabs manufactured components included the *y*-axis linear stage, the *z*-axis linear stage, and the 360° *y*-*z* rotation stage fixed around the *x*-axis, which were all controlled through a Thorlabs controller supported by Kinesis 32 bit v1.14.24 software. The linear *x*-stage was a Zaber manufactured item that had its own Zaber controller supported by Zaber Console v2.6.7.429 software. The system was operated by one PC. Despite the different manufacturers, all the motorized linear and rotation stages were controlled with incremental movement as low as 0.1 μm and ~17.453 mrad, respectively. The default moving velocity was set to be 1 mm/s. Calibration of the stage setup was performed according to the manufacturer's instructions. The *y*-*z* linear stages were accurate within 2 μm with a repeatability of 1 μm. The rotational stage has an accuracy of ±820 μrad and a bidirectional repeatability of ±350 μrad. The accuracy of the *x*-linear stage was within 250 μm over a 1 m range with a repeatability of less than 4 μm.

Two stainless-steel rods with 9.525 mm diameters and length dimensions similar to the SiC-SiC tube specimens (380 mm) were fabricated with tight tolerances (±10 μm) for use as a control specimen. The summary results of these specimen, AB and CD, are documented in Appendix A.

4.3 PROFILOMETER INSPECTION

The profilometry was performed by using a Keyence LS-9030MR 2D optical micrometer that was attached to the linear *y*-arm of the remote-controlled translational stage system, as shown in Figure 13(a). The SiC-SiC tube specimen was installed to rest on tapered end caps attached to the rotation stage and foot mount. The stage and foot mount were vertically aligned as far as possible.

The specimen was positioned so that the engraved line associated with P_1 was facing up and aligned with the starting position (i.e., 0° mark) of the rotation stage. Each scan was performed in the axial direction along the length of the specimen, starting at the rotation stage head and ending at the foot mount (i.e., from the end with the engraved perimeter number, P_x, toward the end with the engraved ID). The micrometer detector is 30 mm wide, and the tube specimens have a ~9.5 mm diameter. Thus, each scan recorded the top profile, the bottom profile, and the diameter. After each scan, the specimen was turned 45° (0.785 rad) to record the profile of each perimeter line.

The profilometer used edge detection to identify the top surface of the specimen and tracked the variation in the profile of this surface as the stage translated along the specimen's length. All profilometry data were postprocessed by using coordinate transformations so that the first and last points—corresponding to the top and bottom of the specimen, respectively—were coplanar, even if the specimen or stage was not perfectly flat.

4.4 OPTICAL IMAGING USED FOR STRAIN MAPPING

Included on the linear *y*-arm of the stage system is a mount for a digital microscope that looks down on the top of the specimen. Two digital microscopes, the Dino-Lite AF4115ZT for low magnification (< 50×) and the Dino-Lite AM73515MT8A for high magnification (>900×), were used to collect digital imagery of the specimens. The low-magnification images were used for panoramic reconstruction to capture unique specimen surface features, and the combination of the high-magnification microscope together with the stage system allowed for the precise determination of the distance between engraved markers.

The high-magnification microscope was used to identify the center of each marker, and the *X*, *Y*, and *Z* coordinates together with the rotation angle from the stage system were recorded for each marker. Figure 13 (b) shows the setup. Each marker is about 25 mm apart along the length of the specimen. For this activity, the specimen was flipped so that the coordinates were recorded, starting at the specimen perimeter number, P_x (positioned to rest on the foot mount), moving toward the specimen end with the engraved number 01 or 22 (positioned to rest on the rotation stage). This allowed for better operator visibility and stage control.

Image analysis can be performed to identify the center of the marker relative to the center of the image more precisely. The displacement measurements are expected to be accurate to within <10 μm, which is limited by the image analysis rather than the accuracy of the stage. A ±10 μm displacement resolution corresponds to a linear strain resolution of ±0.01%. Image processing was done using Fiji [14].

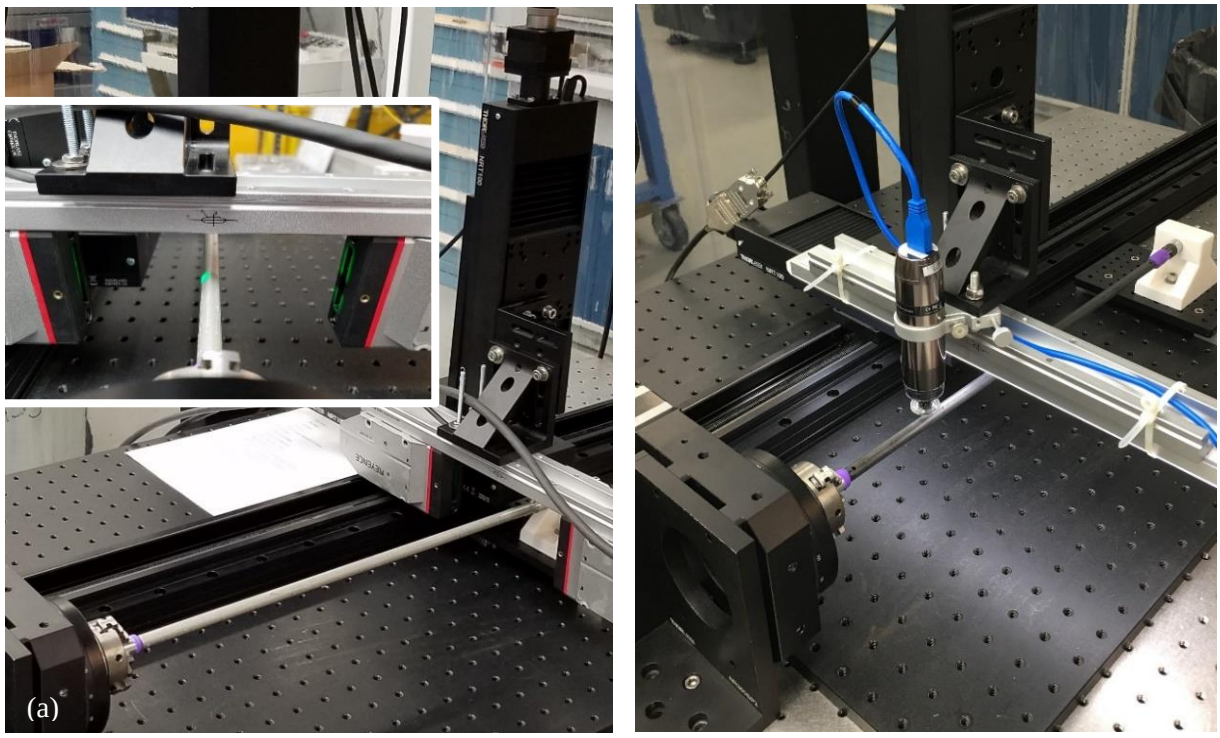

Figure 13. SiC-SiC tube specimen positioned for (a) 2D profile scans with the Keyence Optical Micrometer and (b) local strain measurements using a Dino-Lite high-magnification microscope.

5. PRE-IRRADIATION CHARACTERIZATION

5.1 DIMENSIONAL INSPECTIONS

The results from dimensional inspections are summarized in Table 1. From dimensional inspections, the results show that both specimens were slightly tapered with a nominal difference of 93 and 121 μm from top to bottom for T01 and T22, respectively. The standard deviation of the diameter position D_3 is 0.003 mm for T01 and 0.007 mm for T22. Also, the thickness between the top and bottom varies between 44 and 83 μm on average, respectively. After being cleaned with acetone and ethanol, the masses for T01 and T22 were measured to be 29.800 and 29.497 g, respectively.

Table 1. Summary of nominal dimensions by dimensional inspection in millimeters on T01 and T22 SiC-SiC tube specimens and control specimen AB.

Specimen	L	D_1	D_2	D_3	D_4	D_5	t_{top}	t_{bot}
T01	382.37	9.746	9.753	9.778	9.808	9.839	1.061	1.105
T22	382.51	9.739	9.772	9.792	9.830	9.860	1.062	1.146

* L is length, D_x is diameter at positions 1–5, and t_{top} and t_{bot} are thickness at top and bottom, respectively.

The straightness results are summarized in Table 2 and show the variation from the reference point, P_1-3. The positive values reference the distance above the horizontal zero line in the *z*-direction, and negative values indicate the distance below the horizontal zero line.

Table 2. Straightness measurements of the SiC-SiC tube specimens T01 and T22 in millimeters.

Specimen	P_1-3	P_2-3	P_3-3	P_4-3	P_5-3	P_6-3	P_7-3	P_8-3
T01	0.000	-0.117	-0.133	-0.061	0.062	0.178	0.176	0.122
T22	0.000	-0.087	0.011	0.159	0.469	0.549	0.458	0.283

The height difference (*z*-direction) measured with the aforementioned indicator, shows that the specimens have a slight bow and are not completely straight.

5.2 PROFILOMETRY INSPECTIONS

The detailed profile measurements of the SiC-SiC tube specimens T01 and T22 were scanned after calibration, and control scans were performed with a nominally straight stainless-steel bar to ensure that the system did not introduce significant artifacts into the measurements. After scanning the bar in one direction, the bar was reversed and rescanned. The bar was placed directly on the baseplate so that it was independent of the stage system. A maximum deviation of 28 μm was observed and caused by the stage and the surface on which the part is sitting. The profile variation of the stainless-steel bar was measured to be 3–4 μm by using a dial indicator. This small variation is much less than the expected radiation-induced bowing (Figure 6) and would likely be present in both pre- and post-irradiation measurements. Thereafter, a stainless-steel rod used as a control specimen positioned in a similar fashion as the SiC-SiC tube specimens was scanned. The results of the control specimen and details of the straight bar are reported in Appendix A.

The top profile, bottom profiles, and diameter of each specimen at every 45° rotation angle were recorded with each scan. The diameters of both specimens, T01 and T22, were slightly tapered, as shown in Figure 14. This also validates the results of the dimensional inspections. The result from the 2D laser profiler for specimen T01 (Figure 15) are consistent with the indicator inspections, but there is a large inconsistency with specimen T22 (Figure 16) with a ~0.2 mm difference in the reported straightness. All other dimensions agree with the 2D laser profiler results, so it is more likely an error in the measured indicator results.

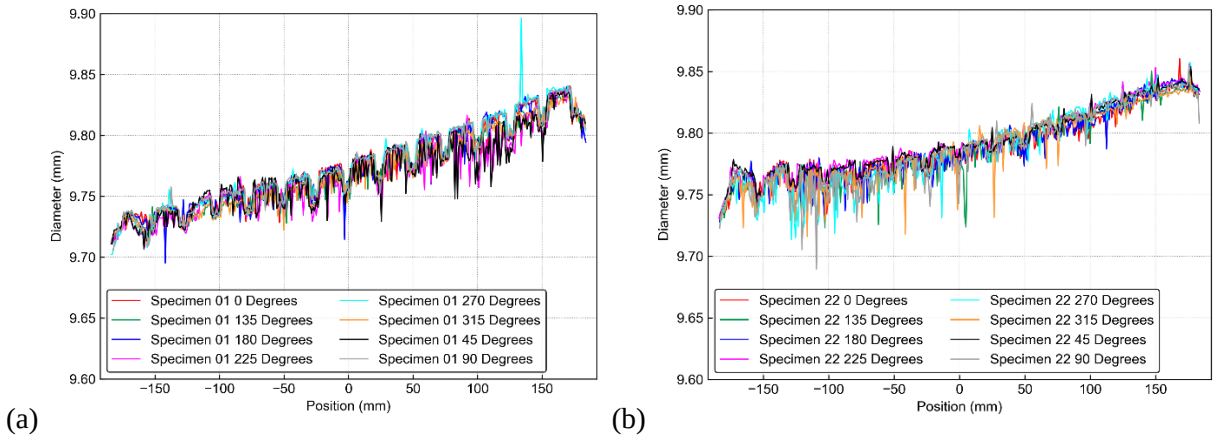

Figure 14. Diameter plots of the SiC-SiC tube specimens (a) T01 and (b) T22 for the eight respective scans.

Figures 15 and 16 show the respective transform plots of the top and bottom profiles of the tube specimens. The top and bottom profiles shown in the plots correspond to the respective bending profile of the top and bottom outer surface of each specimen at the indicated rotation angle so that the 90° profile in Figures 15(a) and 16(a) is equivalent to the inverse profile plot in Figures 15(b) and 16(b), which is shown as the 270° profile.

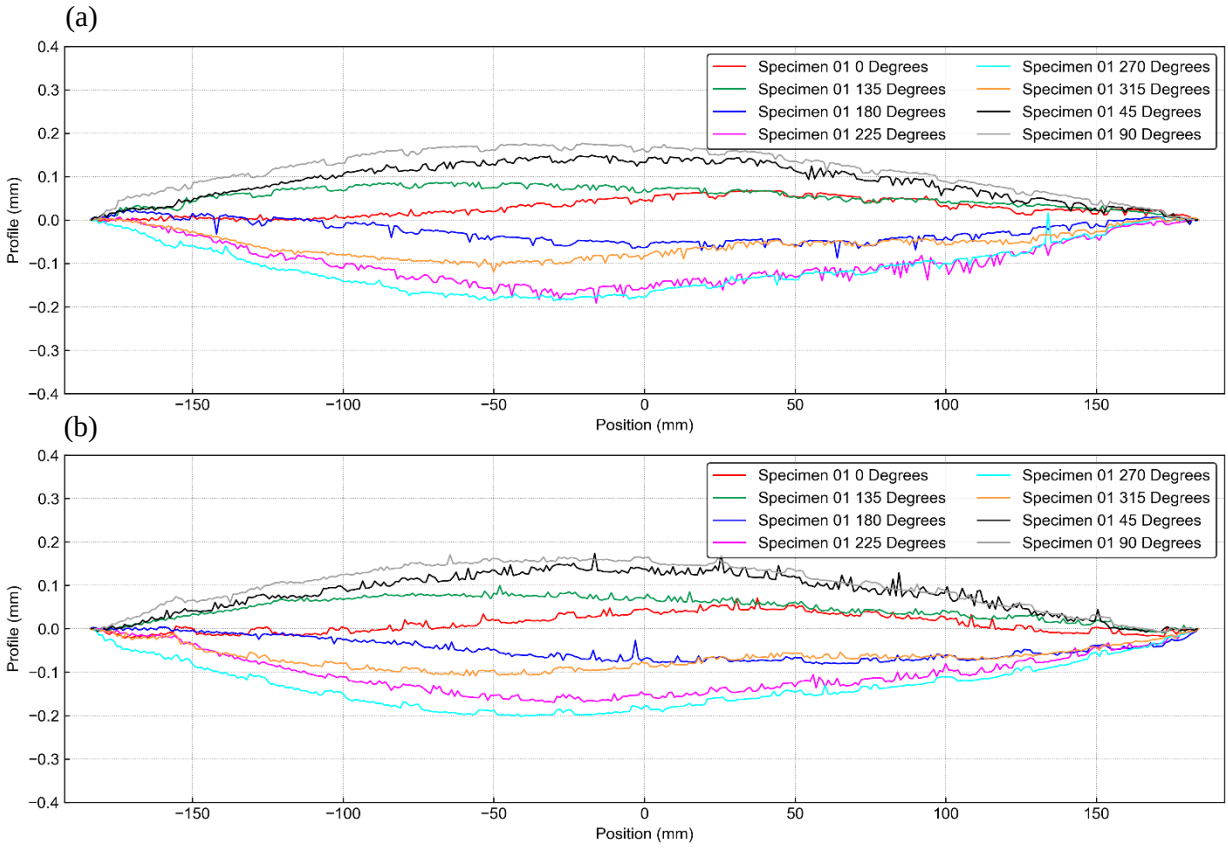

Figure 15. The transformed plot of SiC-SiC tube specimen, T01, showing the (a) top profile and (b) corresponding bottom profile of the eight respective scans.

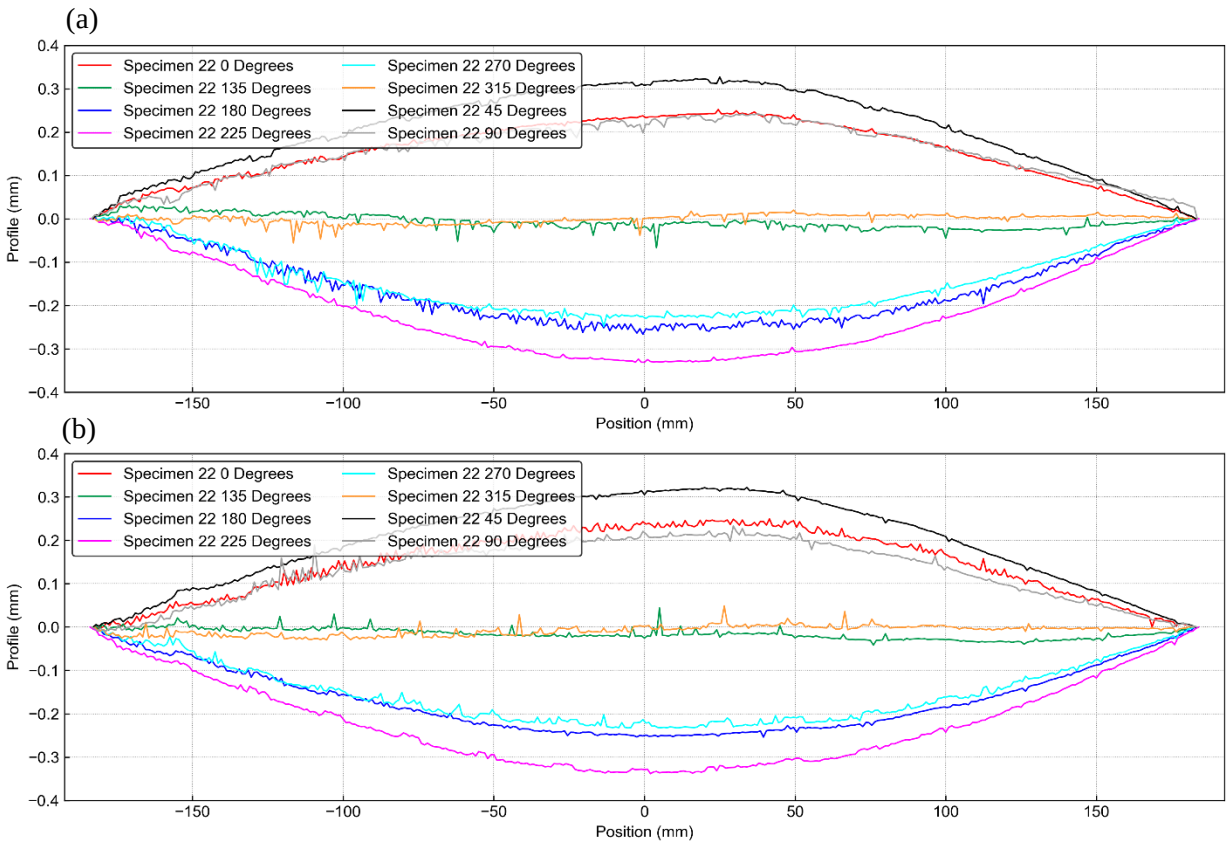

Figure 16. The transformed plot of SiC-SiC tube specimen, T22 showing the (a) top profile and (b) corresponding bottom profile of the eight respective scans.

The position data Z (x-axis) are reversed in these plots so that following the profiles from right to left is equivalent to following the specimen profiles from top to bottom (i.e., from the end marked with the perimeter numbers, P_x, to the end marked with the specimen ID). This is also equivalent to the vertical installation position during irradiation.

5.3 FIDUCIAL MARKER RECORDINGS FOR LOCAL STRAIN MAPPING

Low-magnification images were reconstructed to record closeup views of the specimens, as shown in Figure 17(a). The stage system and the high-magnification microscope were used to locate the center of the fine engraved fiducial marks. Once located, the coordinates were recorded and at each fiducial mark. Several high-magnification images at stepwise height distances from the specimen in 10 μm increments (for better focus through depth of field) were taken and then stacked to create the images shown in Figure 17(b). It is possible to detect specific image features smaller than 5 μm at a resolution of ~6 px/μm by using image analysis techniques.

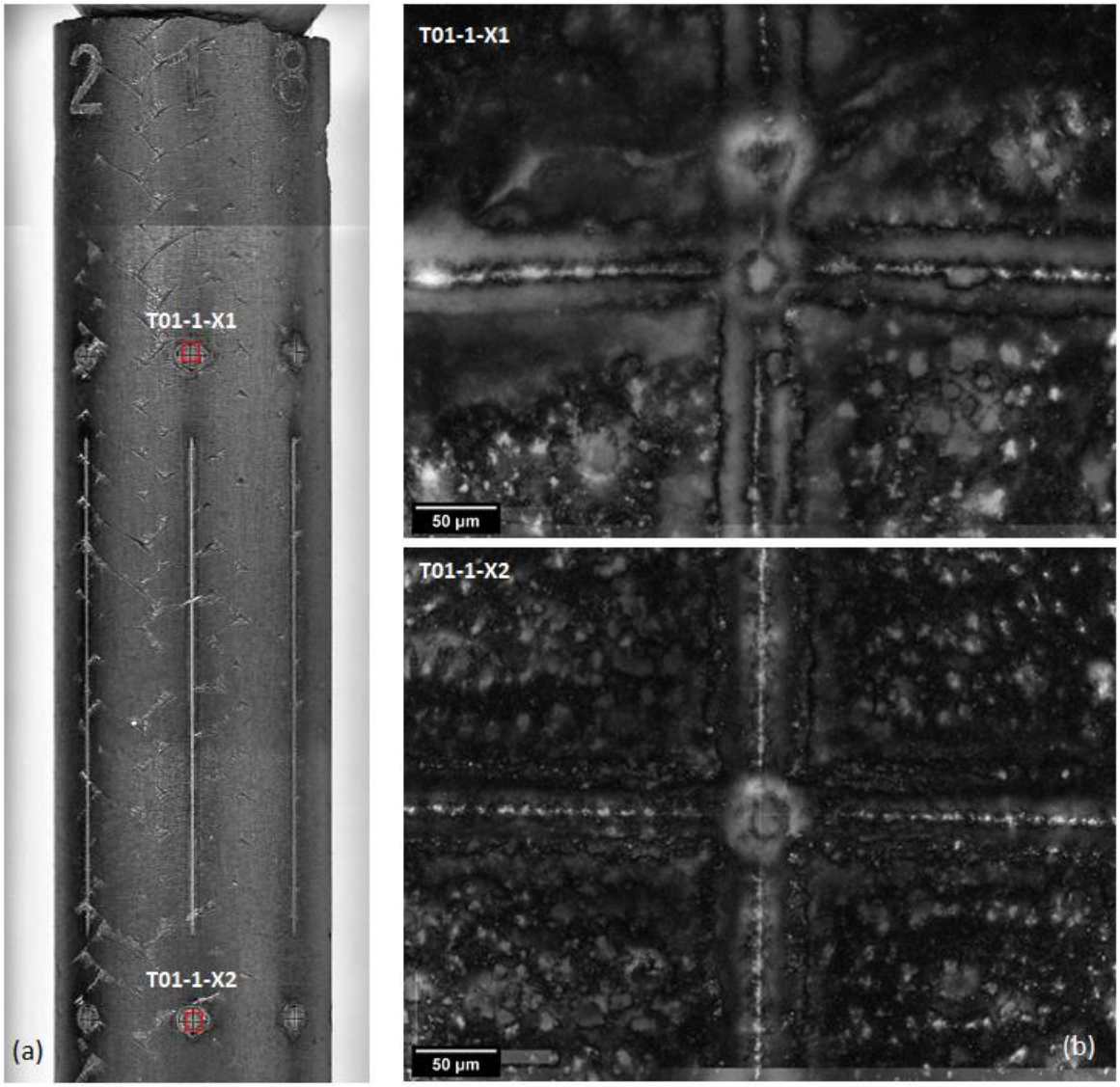

Figure 17. (a) Example of a stitched image section of specimen T01 showing the (b) stacked images created of the engraved fiducial markings T01-1-X1 and T01-1-X2.

Figure 18 shows the respective maps of the recorded coordinates of the engraved fiducial markings on every 45° rotational angle of specimen T01 and T22. The first fiducial mark closest to the engraved perimeter number, P_x, is used as the reference or starting point for the specific series. As the specimen was flipped, the P_x recordings were associated with a counterclockwise rotation angle of the rotation stage, and although the specimen was ~382 mm long, the total distance from the first marker to the last (along the length) was ~355 mm. The exact coordinate details are shown in Appendix B.

In each case, there was a slight drift during the fine engraving procedure because the markers were slightly skewed, deviating in the *y*-direction as the distance away from the starting position increase.

One marker of specimen T01 in the P_4 series was incorrectly recorded. Upon closer investigation, it was observed that the *z*- and *y*-coordinates were switched during the recording. The correction is reflected in the plot, but the specific marker was highlighted.

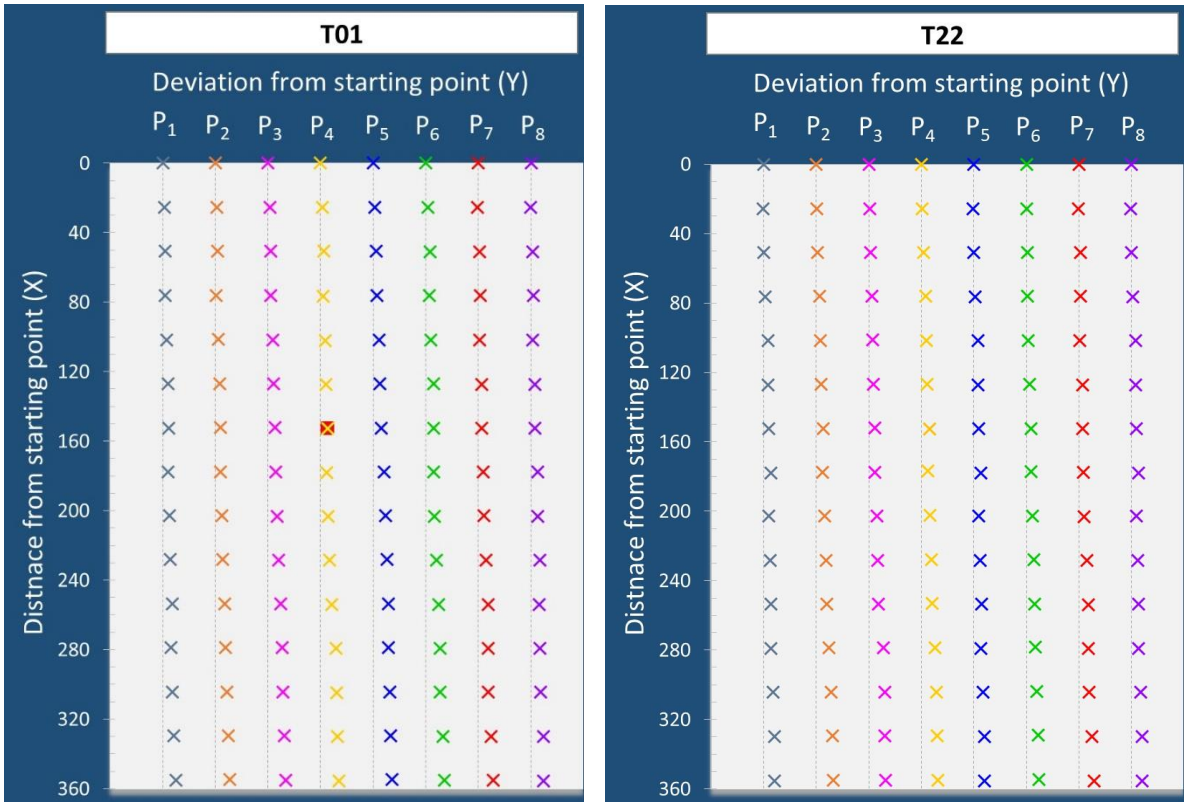

Figure 18. The recorded pre-irradiation fiducial marker plots for specimen T01 (left) and T22 (right) showing markers respective with the associated perimeter number's starting point. Units in millimeters.

6. CONCLUSION

This report summarizes the purpose, experiment design, specimen preparation, and pre-irradiation characterization techniques prepared and applied for the two SiC-SiC clad tube specimens. Both specimens were inspected and characterized before being assembled as part of the channel box bowing experiment for HFIR irradiation.

The dimensional inspection results mostly correspond to the profilometry results with both demonstrating that the two SiC-SiC tube specimens are not completely straight and are slightly tapered in diameter. Specimen T01 has the largest measured bow at the 270° rotational angle—which corresponds to the inverse 90° rotational angle—with a nominal value of 0.2 mm, and T22 has the largest measured bow at the 225° rotational angle—which corresponds to the inverse 45° rotational angle—with a nominal value of 0.35 mm.

The fine engraved fiducial markers were individually measured with respect to the specified reference points by locating the center of the cross marking with the high-magnification images and taking the respective coordinates provided by the stage system.

The experiment completed two HFIR cycle irradiations: cycles 492 and 493. With a two-cycle irradiation, the bow caused by irradiation is anticipated to be 0.8–1.0 mm for the two specimens, depending on the irradiation position (i.e., closer or further from the core).

7. REFERENCES

[1] Katoh, Y., et al., "Continuous SiC fiber, CVI SiC matrix composites for nuclear applications: Properties and irradiation effects". J. Nucl. Mater., 448 (2014) p. 448-476.

[2] Singh, G., et al., "Parametric Evaluation of SiC/SiC Composite Cladding with UO2 Fuel for LWR Applications: Fuel Rod Interactions and Impact of Nonuniform Power Profile in Fuel Rod". J. Nucl. Mater., 499 (2018) p. 155-167.

[3] Christian M. Petrie, Josina W. Geringer, Adam James, Kurt Smith, Joseph R. Burns, Annabelle G. Le Coq, Nicholas Russell, Christian P. Deck, Takaaki Koyanagi, Yutai Katoh, "HFIR SiC Bowing Test Ready to Insert", ORNL Report, ORNL/SPR-2021/1838.

[4] Y. Lee, M.S. Kazimi, "A structural model for multi-layered ceramic cylinders and its application to silicon carbide cladding of light water reactor fuel", J. Nucl. Mater. 458 (2015) p. 87-105.

[5] G.A. Newsome, L.L. Snead, T. Hinoki, Y. Katoh, D. Peters, J. Nucl. Mater. 371 (2007) 76–89.

[6] K. Ozawa, Y. Katoh, L.L. Snead, T. Nozawa, T. Hinoki, A. Hasegawa, The effects of neutron irradiation on dimensional change in advanced silicon carbide composites, DOE/ER-0313/46 Fusion Reactor Materials Semiannual Progress Report for Period Ending June 30, 2009, pp. 4–15.

[7] Y. Katoh, K. Ozawa, S. Shih, T. Nozawa, R. Shinavski, A. Hasegawa, L. Snead, Continuous SiC fiber, CVI SiC matrix composites for nuclear applications: Properties and irradiation effects, Journal of Nucl. Mater. 448 (2014) p. 448-476.

[8] Yutai Katoh, Takashi Nozawa, Chunghao Shih, Kazumi Ozawa, Takaaki Koyanagi, Wally Porter, Lance L. Snead, High-dose neutron irradiation of Hi-Nicalon Type S silicon carbide composites. Part 2: Mechanical and physical properties, J. Nucl. Mater. 462 (2015) p. 450-457.

[9] Y. Katoh, L. Snead, S. Golubov, E. Lara-Curzio, Analyzing irradiation-induced creep of silicon carbide, in: Mechanical Properties and Performance of Engineering Ceramics and Composites III, Wiley, 2007.

[10] Yutai Katoh, Takaaki Koyanagi, Joel L. McDuffee, Lance L. Snead, Ken Yueh, Dimensional stability and anisotropy of SiC and SiC-based composites in transition swelling regime, J. Nucl. Mater. 499 (2018) p. 471-479.

[11] C.M. Petrie, J. McDuffee, N. Cetiner, R. Howard, P. Mulligan, "Nuclear Science User Facilities Irradiation Capabilities at Oak Ridge National Laboratory," Transactions of the American Nuclear Society Vol. 116 (2017) p.377-380.

[12] Christian M. Petrie, Kurt R. Smith, Joseph R. Burns, Annabelle G. Le Coq, Yutai Katoh, Christian P. Deck, "Irradiation Testing of a SiC/SiC Channel Box in the High Flux Isotope Reactor", Oak Ridge National Laboratory, ORNL/TM-2018/957.

[13] C.M. Petrie, J. Burns, C. Deck, Y. Katoh, "Bowing analysis of a SiC/SiC channel box irradiation experiment in the HFIR", ICACC 2019, Daytona Beach, FL, January 2019.

[14] Schindelin, J., Arganda-Carreras, I., Frise, E., Kaynig, V., Longair, M., Pietzsch, T., … Cardona, A. (2012). Fiji: an open-source platform for biological-image analysis. Nature Methods, 9(7), 676–682. doi:10.1038/nmeth.2019

APPENDIX A. INSPECTION RESULTS OF THE STEEL CONTROL SPECIMEN

APPENDIX A. INSPECTION RESULTS OF THE STAINLESS-STEEL CONTROL SPECIMEN

Tight-tolerance (±10 μm), multipurpose 304 stainless-steel rods with a 9.525 mm diameter and length dimensions cut to the size of the SiC-SiC tube specimens (380 mm) were used for control specimens.

The purpose of the control specimens is to validate system performance because the custom 3D translation system will be disassembled. A similar system will be assembled elsewhere to perform post-irradiation evaluation. The system performance will then be validated via control specimens.

Two control specimens, AB and CD, were inspected by applying similar methods, as described in the report. They were not engraved in the same way so that the surfaces remained undisturbed. The ends were slightly tapered to snugly fit the mounting fixtures and marked as shown in Figure A.1.

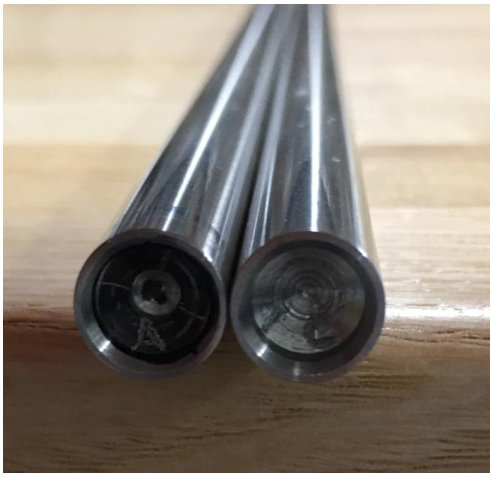

Figure A.1. Control specimen AB and CD with marker lines.

The diameter, cylindricity, and straightness of the respective rods were measured. As with the composite specimens, the straightness was measured at the center of the rod every 45° for positions 1–8. The rods were marked with a red line using a permanent marker to indicate the position where it was measured.

The diameter is consistent throughout the specimen length. This was also confirmed with the profiler scans, which measured the diameter of control specimen, AB, as 9.518 mm with a standard deviation of 4.7×10^{-4} and control specimen, CD, as 9.533 mm with a standard deviation of 6.4×10^{-4}. Both control specimens AB and CD are not perfectly straight and were measured with a maximum deviation of 28 μm for both. The inspection report is shown in Figure A.2.

QC #*	Inspection Result	Drawing Requirement	Inspection Method
		A-B	
A-END	9.522mm	DIAMETER	OUTSIDE MICROMETER
MIDDLE	9.522mm	DIAMETER	OUTSIDE MICROMETER
B-END	9.523mm	DIAMETER	OUTSIDE MICROMETER
	0.031mm	CYLINDRICITY	MITUTOYO RA2200AH
Position 1 (RED DOT UP)	0	STRAIGHTNESS	HEIGHT GAGE
Position 2	-0.006	STRAIGHTNESS	HEIGHT GAGE
Position 3	-0.007	STRAIGHTNESS	HEIGHT GAGE
Position 4	0.003	STRAIGHTNESS	HEIGHT GAGE
Position 5	0.021	STRAIGHTNESS	HEIGHT GAGE
Position 6	0.028	STRAIGHTNESS	HEIGHT GAGE
Position 7	0.022	STRAIGHTNESS	HEIGHT GAGE
Position 8	0.014	STRAIGHTNESS	HEIGHT GAGE
		C-D	
C-END	9.522mm	DIAMETER	OUTSIDE MICROMETER
MIDDLE	9.523mm	DIAMETER	OUTSIDE MICROMETER
D-END	9.522mm	DIAMETER	OUTSIDE MICROMETER
	0.031mm	CYLINDRICITY	MITUTOYO RA2200AH
Position 1 (RED DOT UP)	0	STRAIGHTNESS	HEIGHT GAGE
Position 2	-0.010	STRAIGHTNESS	HEIGHT GAGE
Position 3	-0.011	STRAIGHTNESS	HEIGHT GAGE
Position 4	-0.003	STRAIGHTNESS	HEIGHT GAGE
Position 5	0.018	STRAIGHTNESS	HEIGHT GAGE
Position 6	0.028	STRAIGHTNESS	HEIGHT GAGE
Position 7	0.027	STRAIGHTNESS	HEIGHT GAGE
Position 8	0.017	STRAIGHTNESS	HEIGHT GAGE
The cylindricity measurement was taken at 5 places along the length of the part.			

Figure A.2. Metrology inspection report of control specimens AB and CD.

Figures A.3 and A.4 show the transformed profiles of control specimens AB and CD, respectively. The profiles were force-fitted through zero at the ends. The top and bottom profiles are the top and bottom profile scans while the specimen was positioned at a specific rotational angle, as listed in the graphs.

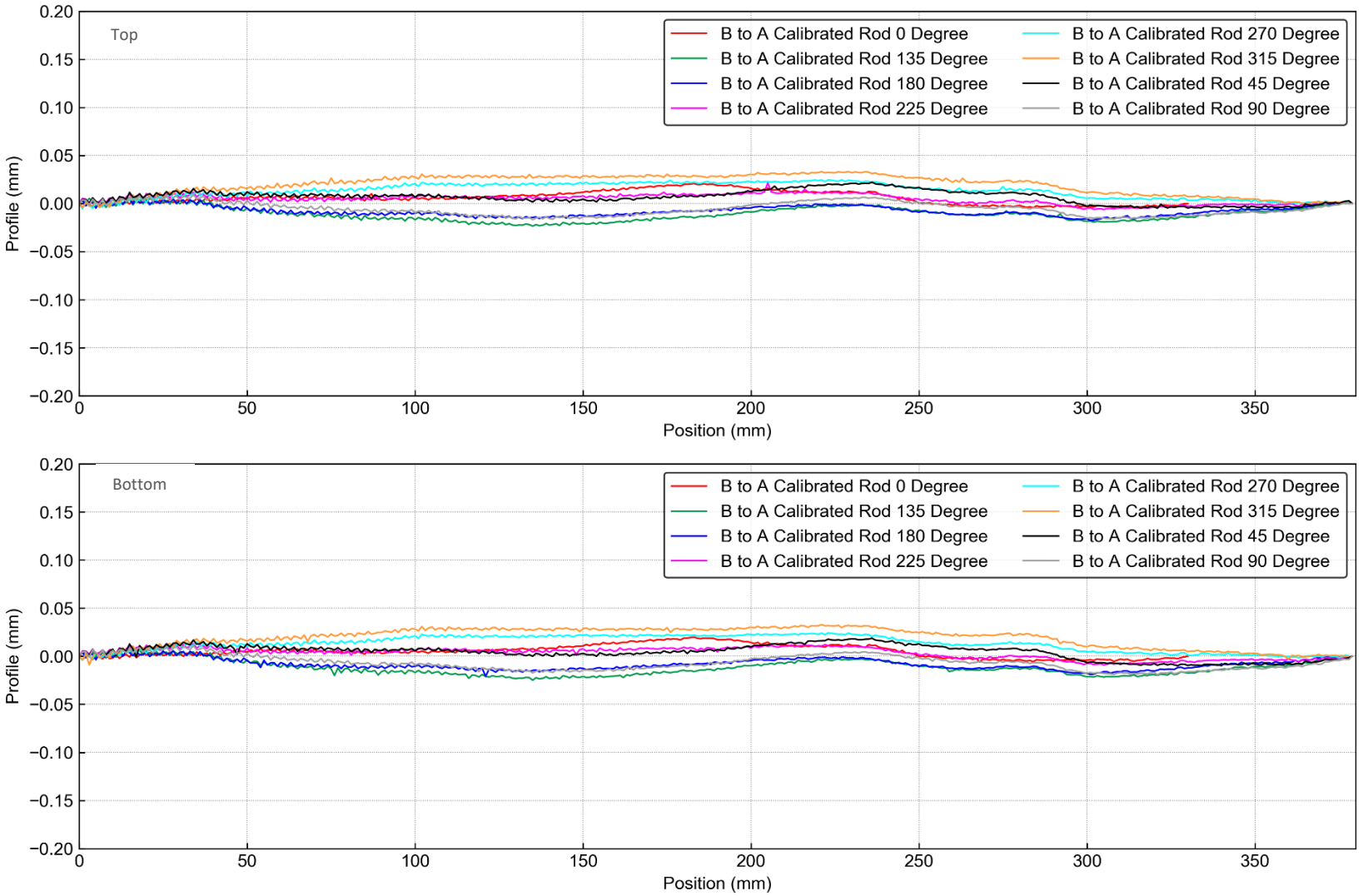

Figure A.3. Transformed profile results (top and bottom) of control rod specimen AB.

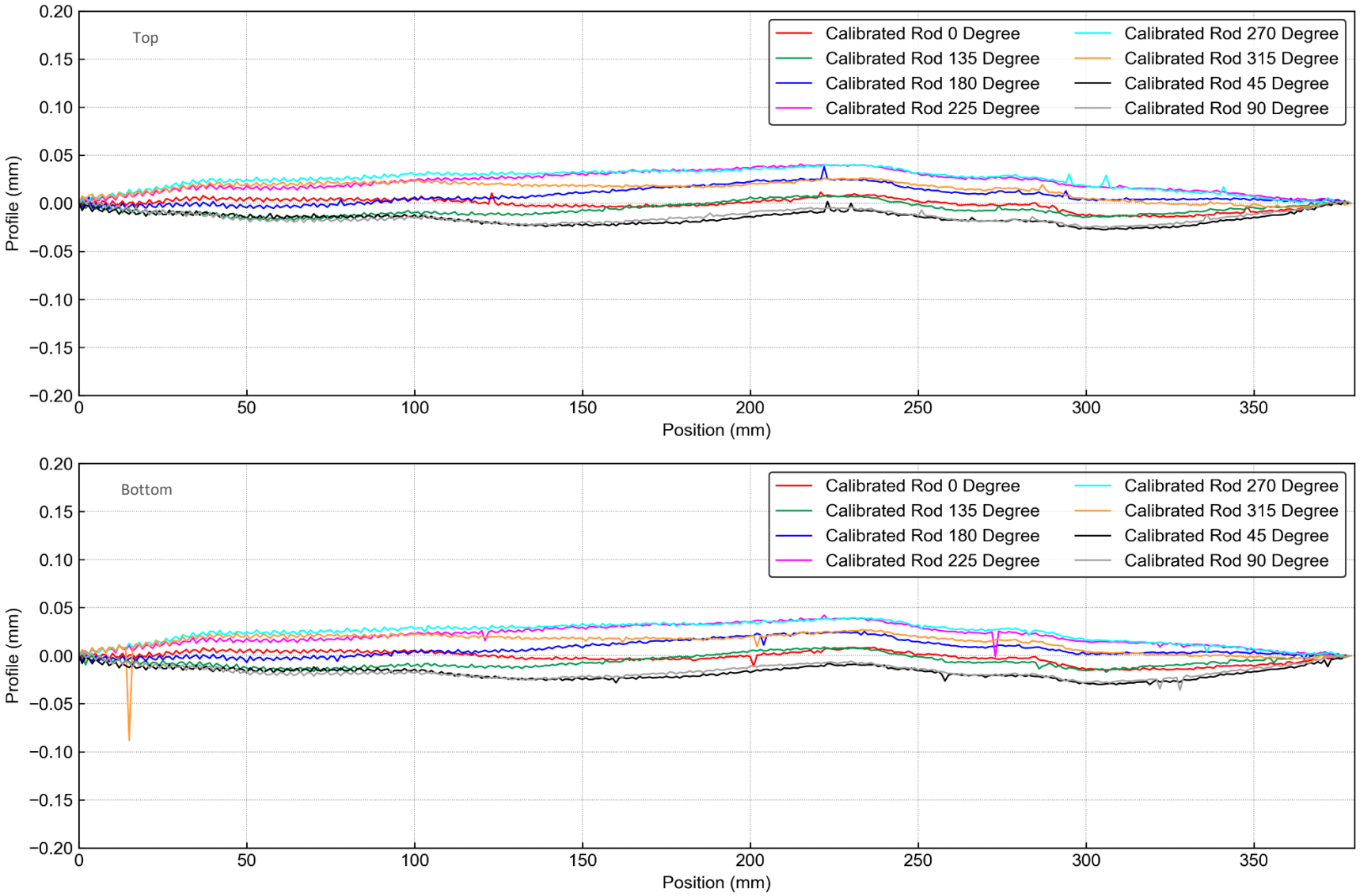

Figure A.4. Transformed profile results (top and bottom) of control rod specimen CD.

Both figures show that all the datasets indicate a gradual increase and a peak near the 225 mm position on the scale. This indicates an artifact, suggesting that the detector's track is not perfectly straight. This was confirmed by using a straight stainless-steel bar that was scanned in one direction and then flipped so that it was rescanned in the reversed direction. Figure A.5 shows the results of the forward scan and reversed scan, which indicates that some small artifact creates a ~25–28 μm deviation. The stainless-steel bar was independently measured to have a straightness of 3–4 μm. This explains the very large profile variation between the indicator-measured straightness and those measured by the 2D laser profiler.

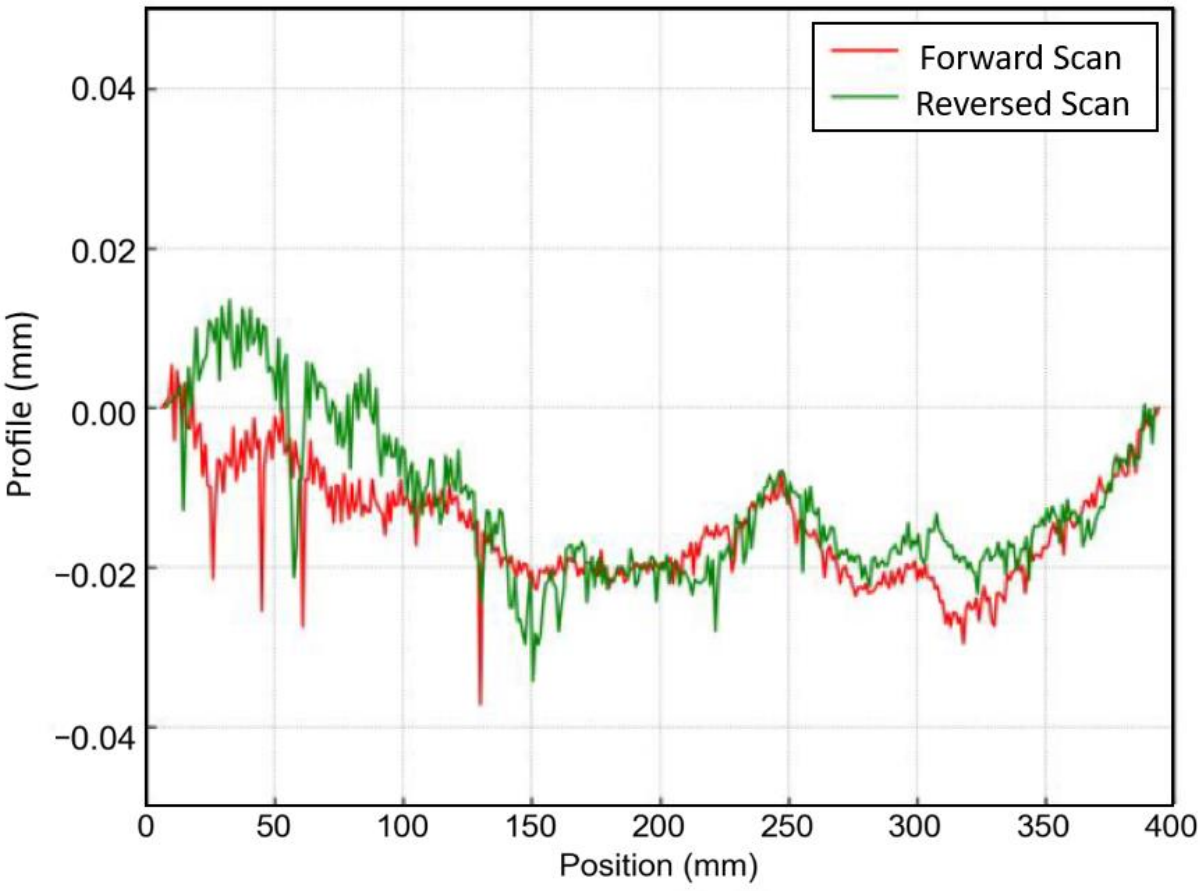

Figure A.5. Forward and reverse scan of a straight bar.

APPENDIX B. MEASURED LOCATIONS OF ENGRAVED MARKERS OF THE SIC-SIC TUBE SPECIMENS

APPENDIX B. MEASURED LOCATIONS OF ENGRAVED MARKERS OF THE SIC-SIC TUBE SPECIMENS

Tables B.1–B.16 show the measured coordinates as retrieved from the translational stage system. For post-irradiation comparison, the marker IDs are labeled with the axial direction (*z*) of the irradiation experiment as it was inserted into HFIR. In each case, the marker "-X1" is the reference closest to the end that is aligned with the top of the reactor, and "-X15" is closest to the end that is aligned with the bottom of the reactor.

Table B.1. Specimen T01, perimeter face P_1 rotational angle: 0.012°.

Marker ID	Axial direction of the tube (mm) [x]	Variable distance from ref. (mm) [y]	Surface normal distance (mm) [z]
T01-1-X1	261.302	92.660	89.470
T01-1-X2	286.738	92.499	89.460
T01-1-X3	311.989	92.419	89.450
T01-1-X4	337.622	92.439	89.430
T01-1-X5	363.056	92.266	89.410
T01-1-X6	388.313	92.170	89.390
T01-1-X7	413.654	92.060	89.380
T01-1-X8	438.880	92.120	89.340
T01-1-X9	464.226	92.019	89.300
T01-1-X10	489.485	91.927	89.260
T01-1-X11	514.918	91.755	89.220
T01-1-X12	540.220	91.871	89.200
T01-1-X13	565.554	91.721	89.170
T01-1-X14	590.807	91.590	89.160
T01-1-X15	616.247	91.386	89.140

Table B.2. Specimen T01, perimeter face P_2, rotational angle: 315.017°.

Marker ID	Axial direction of the tube (mm) [x]	Variable distance from ref. (mm) [y]	Surface normal distance (mm) [z]
T01-2-X1	261.431	92.660	89.470
T01-2-X2	286.857	92.501	89.460
T01-2-X3	312.016	92.430	89.460
T01-2-X4	337.498	92.577	89.480
T01-2-X5	362.952	92.377	89.430
T01-2-X6	388.204	92.272	89.420
T01-2-X7	413.555	92.156	89.440
T01-2-X8	438.999	92.194	89.380
T01-2-X9	464.353	92.060	89.350
T01-2-X10	489.614	91.958	89.300
T01-2-X11	515.050	91.771	89.240
T01-2-X12	540.285	91.682	89.200
T01-2-X13	565.622	91.556	89.150
T01-2-X14	590.869	91.445	89.090
T01-2-X15	616.304	91.266	89.030

Table B.3. Specimen T01, perimeter face P_3 rotational angle: 271.088°.

Marker ID	Axial direction of the tube (mm) [x]	Variable distance from ref. (mm) [y]	Surface normal distance (mm) [z]
T01-3-X1	261.296	92.660	89.540
T01-3-X2	286.727	92.487	89.540
T01-3-X3	311.980	92.396	89.530
T01-3-X4	337.529	92.373	89.520
T01-3-X5	362.963	92.200	89.500
T01-3-X6	388.223	92.101	89.490
T01-3-X7	413.564	91.991	89.480
T01-3-X8	439.041	91.922	89.460
T01-3-X9	464.387	91.790	89.420
T01-3-X10	489.646	91.668	89.360
T01-3-X11	515.085	91.471	89.320
T01-3-X12	540.206	91.328	89.280
T01-3-X13	565.546	91.211	89.220
T01-3-X14	590.802	91.108	89.150
T01-3-X15	616.236	90.936	89.090

Table B.4. Specimen T01, perimeter face P_4 rotational angle: 224.485°.

Marker ID	Axial direction of the tube (mm) [x]	Variable distance from ref. (mm) [y]	Surface normal distance (mm) [z]
T01-4-X1	260.979	92.660	89.620
T01-4-X2	286.410	92.479	89.610
T01-4-X3	311.667	92.382	89.590
T01-4-X4	337.660	92.392	89.590
T01-4-X5	363.096	92.214	89.530
T01-4-X6	388.356	92.120	89.490
T01-4-X7	413.692	92.013	89.470
T01-4-X8	438.979	92.062	89.450
T01-4-X9	464.324	91.932	89.420
T01-4-X10	489.585	91.814	89.380
T01-4-X11	515.021	91.616	89.340
T01-4-X12	540.286	91.221	89.320
T01-4-X13	565.622	91.130	89.290
T01-4-X14	590.876	91.049	89.230
T01-4-X15	616.309	90.897	89.200

Table B.5. Specimen T01, perimeter face P_5 rotational angle: 182.631°.

Marker ID	Axial direction of the tube (mm) [x]	Variable distance from ref. (mm) [y]	Surface normal distance (mm) [z]
T01-5-X1	261.318	92.660	89.680
T01-5-X2	286.757	92.482	89.630
T01-5-X3	312.007	92.387	89.590
T01-5-X4	337.604	92.271	89.550
T01-5-X5	363.044	92.098	89.510
T01-5-X6	388.302	92.007	89.480
T01-5-X7	413.636	91.898	89.460
T01-5-X8	438.895	91.592	89.440
T01-5-X9	464.237	91.472	89.420
T01-5-X10	489.497	91.367	89.410
T01-5-X11	514.939	91.183	89.380
T01-5-X12	540.173	91.193	89.360
T01-5-X13	565.502	91.097	89.350
T01-5-X14	590.754	91.019	89.330
T01-5-X15	616.194	90.866	89.350

Table B.6. Specimen T01, perimeter face P_6 rotational angle: 134.161°.

Marker ID	Axial direction of the tube (mm) [x]	Variable distance from ref. (mm) [y]	Surface normal distance (mm) [z]
T01-6-X1	261.115	92.660	89.760
T01-6-X2	286.549	92.486	89.720
T01-6-X3	311.933	92.263	89.670
T01-6-X4	337.270	92.348	89.620
T01-6-X5	362.708	92.173	89.580
T01-6-X6	388.096	91.936	89.540
T01-6-X7	413.430	91.912	89.510
T01-6-X8	438.866	91.909	89.470
T01-6-X9	464.208	91.872	89.460
T01-6-X10	489.597	91.633	89.430
T01-6-X11	515.039	91.442	89.430
T01-6-X12	540.175	91.311	89.440
T01-6-X13	565.505	91.286	89.450
T01-6-X14	590.888	91.054	89.490
T01-6-X15	616.332	90.888	89.530

Table B.7. Specimen T01, perimeter face P_7 rotational angle: 85.396°.

Marker ID	Axial direction of the tube (mm) [x]	Variable distance from ref. (mm) [y]	Surface normal distance (mm) [z]
T01-7-X1	261.155	92.660	89.740
T01-7-X2	286.711	92.727	89.690
T01-7-X3	312.095	92.519	89.630
T01-7-X4	337.354	92.502	89.620
T01-7-X5	362.915	92.554	89.560
T01-7-X6	388.304	92.333	89.520
T01-7-X7	413.641	92.315	89.490
T01-7-X8	438.804	92.207	89.460
T01-7-X9	464.144	92.171	89.430
T01-7-X10	489.535	91.931	89.400
T01-7-X11	514.978	91.736	89.400
T01-7-X12	540.224	91.753	89.410
T01-7-X13	565.552	91.700	89.440
T01-7-X14	590.932	91.442	89.470
T01-7-X15	616.377	91.239	89.510

Table B.8. Specimen T01, perimeter face P_8 rotational angle: 41.996°.

Marker ID	Axial direction of the tube (mm) [x]	Variable distance from ref. (mm) [y]	Surface normal distance (mm) [z]
T01-8-X1	261.080	92.660	89.650
T01-8-X2	286.638	92.725	89.610
T01-8-X3	312.025	92.516	89.560
T01-8-X4	337.337	92.458	89.530
T01-8-X5	362.898	92.514	89.520
T01-8-X6	388.287	92.301	89.490
T01-8-X7	413.626	92.297	89.460
T01-8-X8	438.929	92.049	89.430
T01-8-X9	464.276	92.045	89.390
T01-8-X10	489.667	91.837	89.360
T01-8-X11	515.235	91.896	89.340
T01-8-X12	540.141	91.789	89.340
T01-8-X13	565.476	91.740	89.340
T01-8-X14	590.861	91.480	89.350
T01-8-X15	616.430	91.500	89.370

Table B.9. Specimen T22, perimeter face P_1 rotational angle: 0.000°.

Marker ID	Axial direction of the tube (mm) [x]	Variable distance from ref. (mm) [y]	Surface normal distance (mm) [z]
T22-1-X1	261.561	92.661	89.572
T22-1-X2	287.156	92.710	89.602
T22-1-X3	312.407	92.662	89.632
T22-1-X4	337.934	92.509	89.662
T22-1-X5	363.205	92.241	89.682
T22-1-X6	388.791	92.276	89.732
T22-1-X7	414.059	92.179	89.672
T22-1-X8	439.589	91.985	89.652
T22-1-X9	464.391	92.210	89.602
T22-1-X10	489.914	92.028	89.572
T22-1-X11	515.172	91.956	89.512
T22-1-X12	540.768	91.980	89.452
T22-1-X13	565.930	91.781	89.392
T22-1-X14	591.184	91.666	89.342
T22-1-X15	616.792	91.666	89.302

Table B.10. Specimen T22, perimeter face P_2 rotational angle: 317.307°.

Marker ID	Axial direction of the tube (mm) [x]	Variable distance from ref. (mm) [y]	Surface normal distance (mm) [z]
T22-2-X1	261.351	92.661	89.690
T22-2-X2	286.859	92.601	89.740
T22-2-X3	312.105	92.525	89.780
T22-2-X4	337.498	92.342	89.810
T22-2-X5	363.001	92.271	89.840
T22-2-X6	388.258	92.188	89.850
T22-2-X7	413.781	92.005	89.850
T22-2-X8	438.721	92.044	89.820
T22-2-X9	464.248	91.840	89.780
T22-2-X10	489.509	91.748	89.730
T22-2-X11	515.022	91.657	89.660
T22-2-X12	540.101	91.451	89.590
T22-2-X13	565.624	91.243	89.527
T22-2-X14	590.877	91.145	89.460
T22-2-X15	616.398	91.057	89.370

Table B.11. Specimen T22, perimeter face P_3 rotational angle: 271.586°.

Marker ID	Axial direction of the tube (mm) [x]	Variable distance from ref. (mm) [y]	Surface normal distance (mm) [z]
T22-3-X1	261.481	92.661	89.670
T22-3-X2	286.991	92.571	89.680
T22-3-X3	312.236	92.472	89.700
T22-3-X4	337.354	92.383	89.710
T22-3-X5	362.864	92.312	89.720
T22-3-X6	388.116	92.247	89.710
T22-3-X7	413.635	92.065	89.710
T22-3-X8	438.854	92.113	89.670
T22-3-X9	464.387	91.915	89.620
T22-3-X10	489.645	91.813	89.580
T22-3-X11	515.157	91.726	89.520
T22-3-X12	540.202	91.298	89.460
T22-3-X13	565.708	91.149	89.390
T22-3-X14	590.949	91.100	89.350
T22-3-X15	616.451	91.065	89.260

Table B.12 Specimen T22, perimeter face P_4 rotational angle: 226.967°.

Marker ID	Axial direction of the tube (mm) [x]	Variable distance from ref. (mm) [y]	Surface normal distance (mm) [z]
T22-4-X1	261.568	92.661	89.720
T22-4-X2	287.081	92.562	89.670
T22-4-X3	312.333	92.457	89.630
T22-4-X4	337.545	92.223	89.600
T22-4-X5	363.062	92.161	89.570
T22-4-X6	388.318	92.085	89.550
T22-4-X7	413.835	91.909	89.520
T22-4-X8	438.483	92.014	89.490
T22-4-X9	464.007	91.807	89.440
T22-4-X10	489.268	91.724	89.410
T22-4-X11	514.787	91.638	89.370
T22-4-X12	540.288	91.375	89.370
T22-4-X13	565.805	91.222	89.320
T22-4-X14	591.059	91.159	89.310
T22-4-X15	616.574	91.118	89.260

Table B.13. Specimen T22, perimeter face P_5 rotational angle: 176°.

Marker ID	Axial direction of the tube (mm) [x]	Variable distance from ref. (mm) [y]	Surface normal distance (mm) [z]
T22-5-X1	261.285	92.661	89.710
T22-5-X2	286.804	92.575	89.610
T22-5-X3	312.055	92.489	89.540
T22-5-X4	337.429	92.198	89.440
T22-5-X5	362.949	92.136	89.380
T22-5-X6	388.204	92.057	89.320
T22-5-X7	413.711	91.878	89.290
T22-5-X8	438.657	92.020	89.260
T22-5-X9	464.174	91.805	89.230
T22-5-X10	489.431	91.690	89.220
T22-5-X11	514.956	91.589	89.200
T22-5-X12	540.030	91.538	89.230
T22-5-X13	565.544	91.376	89.220
T22-5-X14	590.789	91.309	89.240
T22-5-X15	616.314	91.259	89.260

Table B.14. Specimen T22, perimeter face P_6 rotational angle: 131.712°.

Marker ID	Axial direction of the tube (mm) [x]	Variable distance from ref. (mm) [y]	Surface normal distance (mm) [z]
T22-6-X1	261.768	92.661	89.810
T22-6-X2	287.290	92.605	89.700
T22-6-X3	312.543	92.535	89.590
T22-6-X4	337.773	92.538	89.500
T22-6-X5	363.299	92.457	89.420
T22-6-X6	388.561	92.371	89.350
T22-6-X7	414.068	92.185	89.310
T22-6-X8	438.955	92.252	89.280
T22-6-X9	464.471	92.064	89.240
T22-6-X10	489.730	91.970	89.230
T22-6-X11	515.259	91.882	89.230
T22-6-X12	540.078	91.838	89.250
T22-6-X13	565.587	91.645	89.270
T22-6-X14	590.832	91.552	89.310
T22-6-X15	616.356	91.472	89.350

Table B.15 Specimen T22, perimeter face P_7 rotational angle: 85.285°.

Marker ID	Axial direction of the tube (mm) [x]	Variable distance from ref. (mm) [y]	Surface normal distance (mm) [z]
T22-7-X1	261.371	92.661	89.840
T22-7-X2	286.897	92.633	89.750
T22-7-X3	312.148	92.587	89.670
T22-7-X4	337.391	92.407	89.580
T22-7-X5	362.916	92.328	89.520
T22-7-X6	388.172	92.245	89.460
T22-7-X7	413.681	92.061	89.430
T22-7-X8	438.374	92.207	89.400
T22-7-X9	463.897	92.038	89.360
T22-7-X10	489.153	91.968	89.340
T22-7-X11	514.688	91.907	89.370
T22-7-X12	539.969	91.865	89.330
T22-7-X13	565.477	91.655	89.350
T22-7-X14	590.729	91.549	89.370
T22-7-X15	616.255	91.460	89.390

Table B.16. Specimen T22, perimeter face P_8 rotational angle: 40.057°.

Marker ID	Axial direction of the tube (mm) [x]	Variable distance from ref. (mm) [y]	Surface normal distance (mm) [z]
T22-8-X1	261.335	92.661	89.800
T22-8-X2	286.847	92.633	89.770
T22-8-X3	312.097	92.600	89.740
T22-8-X4	337.700	92.471	89.700
T22-8-X5	363.214	92.402	89.680
T22-8-X6	388.470	92.318	89.650
T22-8-X7	413.983	92.136	89.630
T22-8-X8	439.011	92.159	89.590
T22-8-X9	464.535	91.998	89.570
T22-8-X10	489.789	91.934	89.520
T22-8-X11	515.306	91.880	89.480
T22-8-X12	539.740	91.601	89.470
T22-8-X13	565.252	91.373	89.450
T22-8-X14	590.498	91.242	89.430
T22-8-X15	616.020	91.129	89.430